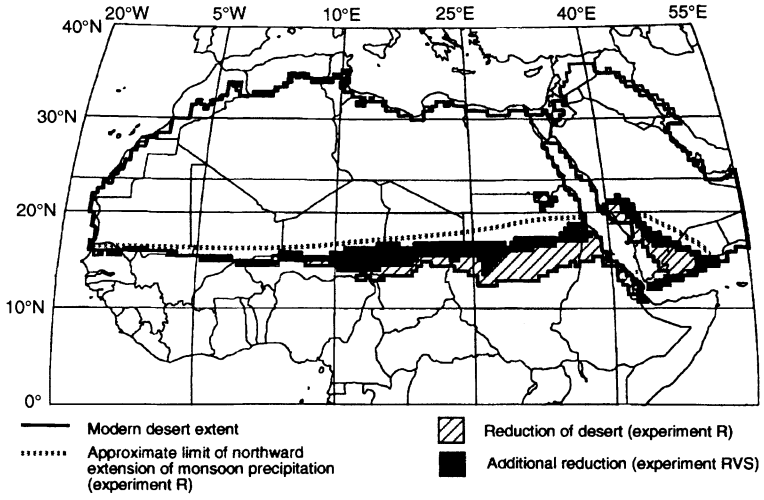

FIG. 3 Location of desert as simulated by a physiologically based biome model[28] driven by output from experiments R and RVS (mean monthly temperature, precipitation, solar radiation), compared to modern. The hatched line marks the approximate limit of northward extension of monsoon precipitation in experiment R. Slant hatching indicates the reduction in the area of desert in experiment R; dark shading indicates the additional reduction in experiment RVS. The shrinking desert is replaced by xerophytic woods/scrub and warm grass/shrub vegetation.

control, R produces a larger area of xerophytic woods/scrub and warm grass/shrub vegetation so that the desert area in the region 0–50° E, 0–30° N, is reduced by 11%; desert is reduced by 16% in RV and 20% in RVS (Fig. 3). The vegetation simulated by RVS is in better agreement with palaeovegetation than that simulated by R (refs 1–4), especially around Lake Chad and eastward into the Sudan where both the simulation and the palaeoenvironmental observations[1–4] indicate vegetation 3° to 5° north of modern limits. None of the simulations produce vegetation in northwest Mali and northeast Sudan as indicated by observations[1–4]. However, it is possible that the northernmost sites record local palaeovegetation rather than a broad continent-wide extension.

Our results and earlier studies[2,7–17] suggest that climate models need to include biospheric processes involving both vegetation and soils. Other factors that might further enhance the climatic response to orbital forcing include the extensive lakes and marshes that existed in northern Africa in the middle Holocene (refs 1–4, and M. T. Coe, personal communication, and changes in ocean circulation that could influence sea surface temperatures. Our results also have implications for the accurate simulation of possible future climates. Climate models simulate changes in African monsoon precipitation in response to increased greenhouse gases[29], but these models will need to include possible vegetation and soil feedbacks to assess more accurately the magnitude of future climate change. □

Received 12 June; accepted 24 October 1996.

1. Street, F. A. & Grove, A. T. *Nature* **261,** 385–390 (1976).
2. Street-Perrott, F. A., Mitchell, J. F. B., Marchand, D. S. & Brunner, J. S. *Trans. R. Soc. Edinb.* **81,** 407–427 (1990).
3. Petit-Maire, N. & Riser, J. *Palaeogeogr. Palaeoclimatol. Palaeoecol.* **35,** 45–61 (1981).
4. Jolly, D., Harrison, S. P., Damnati, B. & Bonnefille, R. *Quat. Sci. Rev.* (in the press).
5. Kutzbach, J. E. & Otto-Bliesner, B. L. *J. Atmos. Sci.* **39,** 1177–1188 (1982).
6. Kutzbach, J. E. & Guetter, P. J. *J. Atmos. Sci.* **43,** 1726–1759 (1986).
7. Mitchell, J. F. B., Grahame, N. S. & Needham, K. H. *J. Geophys. Res.* **93,** 8283–8303 (1988).
8. Bonan, G. B., Pollard, D. & Thompson, S. L. *Nature* **359,** 716–718 (1992).
9. Foley, J., Kutzbach, J. E., Coe, M. T. & Levis, S. *Nature* **371,** 52–54 (1994).
10. Charney, J. G., Quirk, W. J., Chow, S. H. & Kornfeld, J. *J. Atmos. Sci.* **34,** 1366–1385 (1977).
11. Laval, K. & Picon, L. *J. Atmos. Sci.* **43,** 2418–2429 (1986).
12. Xue, Y. & Shukla, J. *J. Clim.* **6,** 2232–2245 (1993).
13. Henderson-Sellers, A. *et al. J. Geophys. Res.* **98,** 7289–7315 (1993).
14. Nobre, C. A., Sellers, P. J. & Shukla, J. *J. Clim.* **4,** 957–988 (1991).
15. Bonan, G. B. *J. Geophys. Rs.* **99,** 25803–25818 (1994).
16. Bonan, G. B. *J. Geophys. Res.* **100,** 2817–2831 (1995).
17. Bonan, G. B. *J. Clim.* **8,** 2691–2704 (1995).
18. Hack, J. J. *et al.* NCAR Technical Note TN-382+STR, 1–108 (National Center for Atmospheric Research, Boulder, CO, 1993).
19. Hack, J. J., Boville, B. A., Kiehl, J. T., Rasch, P. J. & Williamson, D. L. *J. Geophys. Res.* **99,** 20785–20813 (1994).
20. Kiehl, J. T. *J. Geophys. Res.* **99,** 23107–23115 (1994).
21. Berger, A. *J. Atmos. Sci.* **35,** 2362–2367 (1978).
22. Haynes, C. V. *Natl Geogr. Soc. Res. Rep.* **19,** 269–341 (1985).
23. Petit-Maire, N. & Riser, J. *Sahara ou Sahel? Quaternaire récent du Bassin de Taoudenni (Mali)* (Lamy, Marseille, 1983).
24. Milly, P. C. D. & Dunne, K. A. *J. Clim.* **7,** 506–526 (1994).
25. Kutzbach, J. E. *et al. Quat. Sci. Rev.* (in the press).
26. Sperber, K. R. Hameed, S., Potter, G. L. & Boyle, J. S. PCMDI Rep. No. 12, UCRL-ID-11532 (Lawrence Livermore National Laboratory, Livermore, CA, 1993).
27. Boyle, J. S. *J. Clim.* **6,** 796–815 (1993).
28. Prentice, I. C. *et al. J. Biogeogr.* **19,** 117–134 (1992).
29. Mitchell, J. F. B., Manabe, S., Meleshko, V. & Tokioka, T. in *Climate Change: The IPCC Scientific Assessment* (eds Houghton, J. T., Jenkins, G. J. & Ephraums, J. J.) 131–172 (Cambridge Univ. Press, Cambridge, 1990).
30. Legates, D. R. & Willmott, C. J. *Theor. Appl. Climatol.* **41,** 11–21 (1990).
31. Legates, D. R. & Willmott, C. J. *Int. J. Climatol.* **10,** 111–127 (1990).

ACKNOWLEDGEMENTS. We thank P. Behling, R. Selin and J. Kruepke for assistance with model simulations and graphics, and M. Kennedy for preparing the manuscript. This research was supported by grants to the University of Wisconsin–Madison by the NSF Climate Dynamics Program, and the Department of Energy, by the National Center for Atmospheric Research, which is sponsored by the NSF, and by awards to Lund University from the European Community, the Swedish Natural Science Research Council, and the Craaford Fund.

CORRESPONDENCE should be addressed to J. K. (e-mail: jek@facstaff.wisc.edu).

Leading-edge vortices in insect flight

Charles P. Ellington, Coen van den Berg*, Alexander P. Willmott* & Adrian L. R. Thomas*

Department of Zoology, University of Cambridge, Downing Street, Cambridge, CB2 3EJ, UK

INSECTS cannot fly, according to the conventional laws of aerodynamics: during flapping flight, their wings produce more lift than during steady motion at the same velocities and angles of attack[1–5]. Measured instantaneous lift forces also show qualitative and quantitative disagreement with the forces predicted by conventional aerodynamic theories[6–9]. The importance of high-life aerodynamic mechanisms is now widely recognized but, except for the specialized fling mechanism used by some insect species[1,10–13], the source of extra lift remains unknown. We have now visualized the airflow around the wings of the hawkmoth *Manduca sexta* and a 'hovering' large mechanical model—the flapper. An intense leading-edge vortex was found on the downstroke, of sufficient strength to explain the high-lift forces. The vortex is created by dynamic stall, and not by the rotational lift mechanisms that have been postulated for insect flight[14–16]. The vortex spirals out towards the wingtip with a spanwise velocity comparable to the flapping velocity. The three-dimensional flow is similar to the conical leading-edge vortex found on delta wings, with the spanwise flow stabilizing the vortex.

Several studies have visualized the airflow around flapping

* Present addresses: Faculty of Human Movement Sciences, Vrije Universiteit, Van der Boechorststraat 9, 1081 BT Amsterdam, The Netherlands (C.v.d.B.); Kawachi Millibioflight Project, Japan Science and Technology Corporation (JST), Park Building 3F, 4-7-6 Komaba, Meguro-ku, Tokyo 153, Japan (A.P.W.); Department of Zoology, University of Oxford, South Parks Road, Oxford OX1 3PS, UK (A.L.R.T.).

insect wings in an attempt to identify high-lift mechanisms[17–22]. These studies have used planar or sheet illumination with smoke or particles to visualize cross-sections of the flow. The three-dimensional flow field can be reconstructed from a series of such images, but flow normal to the planes is difficult to detect. We therefore used stereophotography to record the three-dimensional flow of smoke around the wings of the hawkmoth *Manduca sexta* tethered in a windtunnel; to our knowledge, this is the first study in which medium and high speeds were investigated in addition to low speeds. *Manduca* has a wing motion typical of many insects, and the downstroke is primarily responsible for weight support. A vertical smoke rake was position on the wind-tunnel axis, and different spanwise positions were examined by moving the tethered moth relative to the smoke (described in detail elsewhere[23]).

Figure 1*a* shows the flow just after the middle of the downstroke, with the plane of smoke filaments halfway along the left forewing (airspeed is 3.7 m s^{-1}). The flow separates at the leading edge and reattaches to the upper surface in the posterior half of the wing, enclosing a leading-edge vortex. Results with the smoke at other spanwise positions show a gradual enlargement of the vortex towards the wingtip. It is reasonable well structured until the outer quarter of the wing, where it breaks away and rolls up into a large diameter tip vortex. As smoke reattaches behind the leading-edge vortex, it changes direction abruptly and flows towards the wingtip and into the tip vortex. The tip vortex runs back to the starting vortex shed at the beginning of the downstroke, which is not visualized with the smoke rake at this location. The tip vortex is most clearly seen early in the downstroke, where the wingtip cuts through the smoke. Figure 1*b* is a stereo drawing that traces the path of the leading-edge/tip vortex.

The leading-edge vortex is a region of low pressure above the wing and thus will augment the lift force. The extra lift can also be explained as an enhanced circulation around the wing due to the vortex; the circulation is a measure of the velocity difference above and below the wing. The two explanations—pressure and circulation—are equivalent. Most of the unsteady aerodynamic mechanisms that have been proposed for insect flight feature lift enhancement by a leading-edge vortex[10–16,24,25], and experiments on rigid, model wings have confirmed that they are potentially effective for two-dimensional wing motions: that is, linear translation with rotation about a spanwise axis (reviewed in ref. 16). Given the size and speed of the wings (a Reynolds number of $\sim 10^3$) and their thin leading edge, flow separation at the leading edge and subsequent reattachment of a large, laminar vortex is almost inevitable.

However, evidence for the vortex from earlier insect studies is limited; the vortex is either not present or otherwise is much smaller than expected[17–22]. It has even been suggested that leading-edge separation is prevented by wing surface microstructure or deformation[21]. We observed the leading-edge vortex at all flight speeds, from 0.4 to 5.7 m s^{-1} (Fig. 1*c*). It is very small, only a fraction of the chord, at 0.4 m s^{-1}; note that the wake is unstable and quickly breaks down at that speed. Studies that failed to observe the vortex used particle visualization in still air[20,21]; the experimental technique was probably inadequate to see the small vortices. None of the earlier studies investigated the flow at medium and high speeds. The size of the vortex increases markedly with speed for *Manduca*, until at 5.7 m s^{-1} it extends over the entire chord. At all speeds, the size increases significantly during the course of the downstroke.

Although these results clearly reveal a leading-edge vortex, they do not identify the aerodynamic mechanism responsible for its creation: the vortex is a common feature of most high-life mechanisms that have been postulated for insect flight. These mechanisms can be divided conveniently into those applicable to the translational phase of the wingbeat, when the fundamental flapping motion imparts a curvilinear motion to the wing elements, and those relevant to the rotational phase at either end of the wingbeat, when the angle of attack changes quickly in preparation for the next half-stroke[16]. Dynamic stall, or delayed stall, is the mechanism appropriate to the translational phase: a wing can travel at high angles of attack for a brief period, generating extra lift with a large leading-edge vortex, before it stalls. For the rotational mechanisms, a leading-edge vortex is created as the wing flips over in preparation for the subsequent half-stroke. The wing is thought to recapture this vorticity upon translation and thus to enhance its circulation. In principle, the pattern of vortex shedding should readily distinguish between the two classes of mechanisms: if the leading-edge vortex is created during the course of downstroke, then dynamic stall is operating; if the vortex is created as the wing flips over during pronation but stays attached on the downstroke, then rotational mechanisms are implicated.

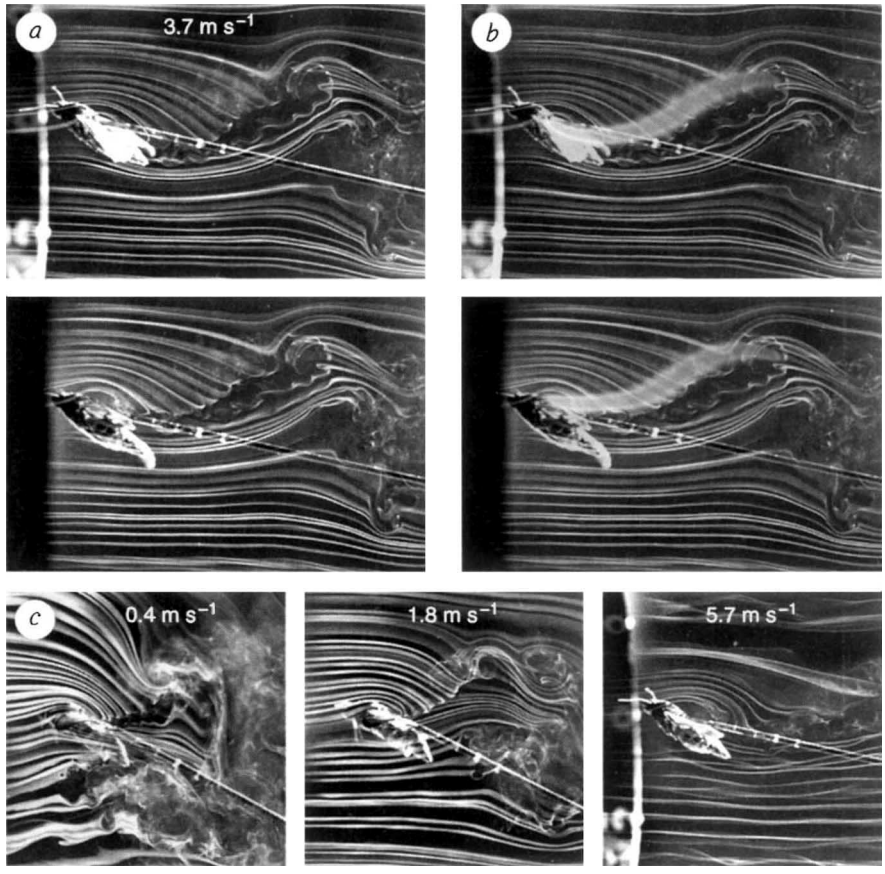

FIG. 1 Flow visualization around a female hawkmoth (mass 1.83 g) late in the downstroke. *a*, Stereo pair at 3.7 m s^{-1}; *b*, stereo drawing superimposed on *a* to trace the main vortex structures; the top and bottom images correspond to the right- and left-hand views, respectively, in this stereo layout. *c*, Changes in the size of the leading-edge vortex at other speeds (0.4, 1.8 and 5.7 m s^{-1}).

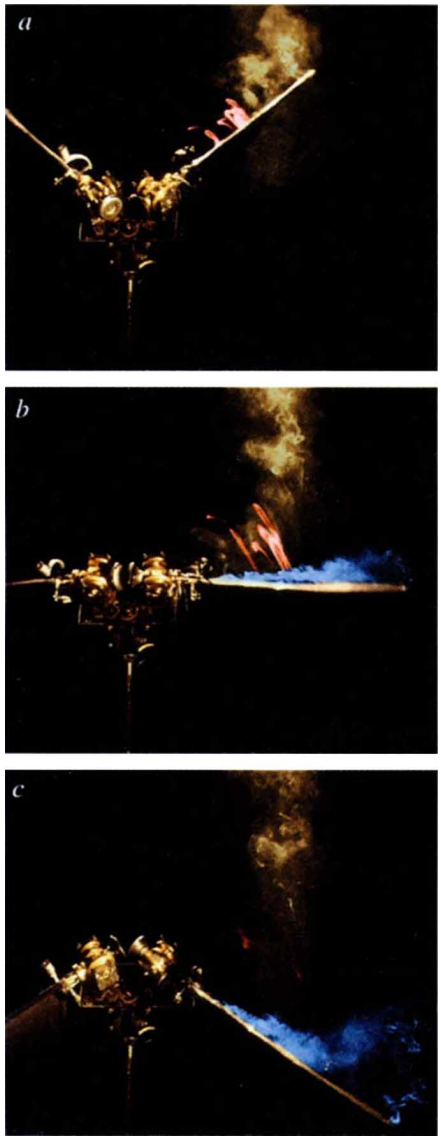

FIG. 2 Flapper flow visualization with smoke released from the leading edge over the inner half of one wing. The camera view is from above and in front of the 'hovering' flapper, parallel to the wing surfaces on the downstroke. *a*, At the end of pronation; *b*, just after the middle of the downstroke; c, near the end of the downstroke. The leading-edge vortex formed during pronation (red) is not recaptured by the wing, and a new leading-edge vortex (blue) is created during the translational phase of the downstroke. During the latter half of the downstroke, the core of the leading-edge vortex breaks down at 60–70% of the wing length and separates from the wing.

Unfortunately, the flow visualization results for tethered insects are not so clear-cut because of the difficulty in obtaining good flow visualization near the wings. To investigate the flow in more detail, we therefore built a three-dimensional mechanical model that closely mimics the wing movements of a hovering *Manduca*. This 'flapper' facilitated visualization by releasing smoke from the leading edge of the wing right into the core of the vortex (for further details, see refs 26, 27).

The model, with a 1.03-m wingspan, is about ten times larger than *Manduca*. To preserve aerodynamic similarity, a wingbeat frequency of 0.3 Hz was used to keep the Reynolds number constant (the ratio of inertial to viscous forces in the air): the frequency of *Manduca* is about 26 Hz. Another similarity condition that might prove important was also met. During a downstroke, the high angle of attack of the wings might cause free vortex shedding, which occurs at a frequency determined by the Strouhal number. For a hovering model at a given Reynolds number, the frequency of free vortex shedding is proportional to the wingbeat frequency. Thus the timing of any free vortex shedding is not altered relative to the forced vortex shedding imposed by the wingbeat. Any second-order patterns of vortex shedding for the flapper should therefore be similar to those for *Manduca*.

Flow visualization results with the 'hovering' flapper clearly identify dynamic stall as the high-lift mechanism. Figure 2 shows a downstroke, filmed obliquely from above and in front. Smoke was released from the leading edge over the inner half of one wing. Figure 2*a* is at the end of pronation, the rotation that precedes the downstroke; the leading-edge vortex formed as the air curled around the leading edge is coloured red, and the smoke remaining from the upstroke is uncoloured. The leading-edge vortex of pronation is quite two-dimensional in structure, with the swirls confined to planes perpendicular to the wing length. During the course of the downstroke, however, this vortex is left behind (Fig. 2*b*, *c*); the leading-edge vortex of pronation is not recaptured by the wing. A new leading-edge vortex, coloured blue, is instead created by the translational motion of the downstroke.

This leading-edge vortex appears at the beginning of the downstroke and persists until the end. As with the *Manduca* results, it grows larger during the course of the downstroke and towards the wingtip. Figure 3 shows the diameter and location of the vortex, as measured in light-slice experiments, for a time corresponding to that in Fig. 2*b*. The leading-edge vortex is a conical spiral, enlarging as it is swept along the wing by an axial (spanwise) flow. Under favourable conditions, the helix angle of clearly defined streaklines in the vortex could be measured. From photographs, the helix angle was estimated to be 46° (s.e.m. = 3°; $n = 15$) with no significant spanwise changes. The magnitude of the axial flow was measured by manually releasing 'blobs' of smoke near the wing base and tracking their positions in video sequences. The axial velocity V_a increased steadily along the inner half of the wing, but then declined and became more variable (Fig. 4). The magnitude of the axial velocities was surprisingly large: near the maximum, values of V_a were fully comparable with the mean wingtip velocity, about 0.5 m s^{-1}.

The downstroke leading-edge vortex is stable and remains attached along the wing until just after the middle of the downstroke (Fig. 2*b*). The vortex core then appears to break down at about 60–70% of the wing length, and the tip region separates from the wing during the latter half of the downstroke (Fig. 2*c*). The variability in V_a (Fig. 4) over this wing region is probably attributable to the vortex breakdown and separation. The separated vortex feeds into a large tip vortex, which also agrees with the *Manduca* visualization results. The cause of vortex core breakdown is unclear, but it corresponds temporally with the onset of wing deceleration after the middle of the downstroke. Spatially, it coincides with the point where the leading edge begins to rake back in *Manduca*, and where the trailing edge bows out because of the hindwing: these planform characteristics can be seen in Fig. 3.

The swirl velocity of the leading-edge vortex could not be measured in light-slice experiments, because the smoke blobs moved out of the slices too quickly. However, the swirl velocity must be equal to the axial velocity because the helix pitch angle is almost 45°. By combining this value with measurements of the vortex diameter, as in Fig. 3, the circulation Γ_{le} of the leading-edge vortex can be calculated. Results are shown in Fig. 5 for the early, middle and late downstroke; the early stage is soon after Fig. 2*a*, whereas the middle and late stages roughly correspond to Fig. 2*b* and *c*, respectively. The circulation clearly increases during the first half of the downstroke, which is consistent with dynamic stall but not with the recaptured vortex of rotational lift mechanisms. The circulation decreases over the outer wing region in the late

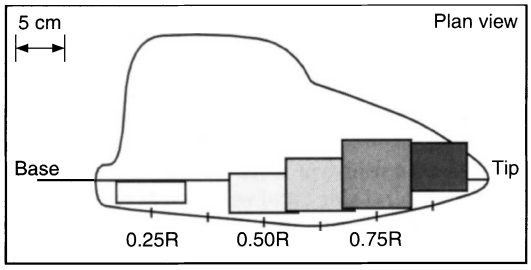

FIG. 3 Planform view of the wing, showing sections of the leading-edge vortex at five spanwise locations (as fractions of the winglength *R*) just after the middle of the downstroke, as in Fig. 2*b*. Sections were illuminated by a 7-cm-wide light slice perpendicular to the wing axis; the dimensions of each pattern show the width of the slice, the vortex diameter and its position on the planform. The leading-edge vortex is a conical spiral, enlarging as it is swept along the wing by the axial flow. The vortex separates from the wing near the wingtip, joining up with the tip vortex, and at 0.87*R* it has lifted away from the wing surface.

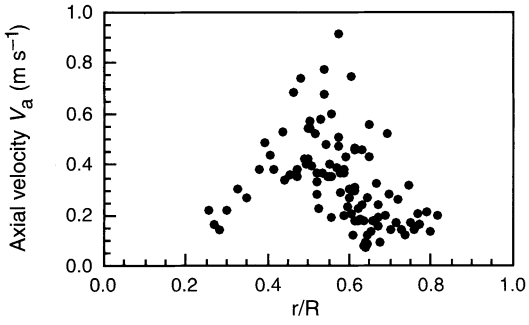

FIG. 4 Axial (spanwise) velocity V_a in the leading-edge vortex, estimated by tracking 'blobs' of smoke released from the wing base. The blobs reached different radial positions *r* (expressed as a fraction of the winglength *R*) at various stages of the downstroke; results are pooled for the whole downstroke.

downstroke, a result of breakdown and separation of the leading-edge vortex.

The spanwise variation of circulation is also consistent with dynamic stall but not the rotational mechanisms. For dynamic stall, the circulation should be proportional to the product *rc*, where *r* is radial position and *c* is the local chord; for rotational mechanisms, circulation should be proportional to c^2 (ref. 15). These two alternatives are shown in Fig. 5, scaled to give the same lift in the middle of the downstroke. The measured circulation for the middle of the downstroke agrees very well with dynamic stall, and the large circulation over the inner half of the wing that would result from rotational mechanisms is absent.

Direct observation of the patterns of vortex shedding, the growth of circulation early in the downstroke, and the spanwise variation in circulation all point unequivocally to dynamic stall as the aerodynamic mechanism responsible for the downstroke leading-edge vortex. Is this vortex strong enough to explain the high lift required for hovering *Manduca*? The wake of the flapper has been analysed in a separate study[26], and the momentum imparted to the air corresponds to a mean lift force on the downstroke of about 1.5 times the weight of *Manduca*. The scaling of winglength and frequency for the flapper will leave the aerodynamic forces unchanged, so this is the same force that *Manduca* should generate. The magnitude of the downstroke lift is, therefore, more than adequate.

Lift enhancement by the spiral leading-edge vortex bears several similarities to the high-lift devices employed on certain man-made wings. The potential of 'attached' vortices to augment lift has long been recognized in aerodynamics, but an axial (spanwise) flow component is essential for the stability of such vortices (reviewed in ref. 28). By convecting the vorticity out to the wingtip, this flow prevents it from accumulating into a large vortex that would be unstable under two-dimensional conditions. The axial flow can be induced by active spanwise suction or blowing over the upper wing surface; for delta wings, it is created instead by the flow component parallel to the swept leading edge. The conical, spiral vortex of the flapper is, in fact, remarkably similar in form to that over delta wings[27]. However, the mechanism of vortex generation for stationary, swept delta wings is quite different from that for hovering insects with flapping, non-swept wings.

Axial flow in the leading-edge vortex has not been observed in previous two-dimensional experiments relevant to insect flight, but the spanwise pressure gradient necessary to drive the axial flow is, by definition, absent in two-dimensional studies. Maxworth's[10] three-dimensional model of the specialized fling motion is the only other case where axial flow has been reported, and it now seems likely that this three-dimensional flow pattern is a common feature of insect flight. It seems reasonable to assume that the flow is generated either by the dynamic pressure gradient associated with the velocity gradient along the flapping wing, by 'centrifugal' acceleration in the boundary layer, or by the induced velocity field of the spiral vortex lines. Helicopter rotors and windturbine blades also experience such spanwise pressure gradients and centrifugal accelerations, but large-scale spanwise flows have not been observed[29]; however, there is some evidence that a spanwise flow influences their stall characteristics[30]. It may be that the Reynolds numbers are too high for a large leading-edge vortex to persist, or that the spanwise flow component is reduced for high-aspect-ratio airfoils like helicopter blades. The exact conditions for establishing axial flow in a leading-edge vortex for rotary wings are not yet understood. □

Methods

Hawkmoth visualization. Moths were tethered 5 cm downstream from a 26-cm-diameter open jet wind-tunnel. The body orientation was set to that recorded by high-speed video (Kodak EktaPro 1000, operating at 1,000 frames per second) during free, feeding flights in the wind-tunnel at the same speeds. The tether was mounted on a balance, and experiments were rejected if the moth did not support at least 70% of its weight. Smoke was produced by an FVSP/E smoke generator (Nutem) with medicinal white oil (Shell Ondina EL). Stereo photographs were recorded on two Nikon F3 cameras with optical axes converging by 10°. Illumination was provided by four strobe lamps, and the cameras were set at *f*2.8 and 1/30 s. Ilford HP5 Plus film was processed at 1600 ASA with Microphen developer.

Flapper. The flapper body houses four servo motors and an elaborate gearbox to drive the wing movements, which are mechanically coupled for the left and right wings. As the hawkmoth is a functionally two-winged insect, the fore- and hindwing are constructed as one wing. The wings (2.3 mm thick) consist of a venation-like framework of brass tubes, with rigid and flexible joints as appropriate, covered on both sides with black, elastic cloth. A stiff brass smoke

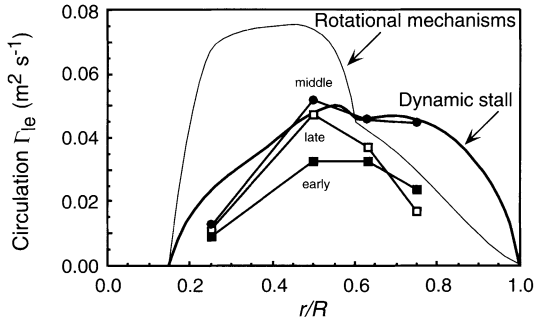

FIG. 5 Estimates of the circulation Γ_{le} of the leading-edge vortex at four spanwise positions for the early, middle and late downstroke. Circulation distributions corresponding to dynamic stall and the rotational mechanisms are also drawn, scaled to give the same lift as Γ_{le} at the middle of the downstroke.

rake extends along the leading edge, and a flexible wire along the trailing edge. Two servos set the angles of attack for the relatively stiff leading edge/wingtip region and for the more flexible trailing edge region. The other two servos flap the wings about their bases, and elevate them perpendicular to the flapping plane. Wing movements were controlled by a Macintosh Quadra 650 computer with D-A converters (NB-A06, National Instruments); custom software was written in LabView 3.0. Kinematic data for a hovering *Manduca* were taken from A.P.W. and C.P.E., manuscript in preparation. Photographic images were scanned and the smoke was then coloured in Photoshop 3.0.

Circulation estimates. Γ_{le} was calculated as $\pi d V_\theta$, where d is the diameter and V_θ is the swirl velocity of the leading-edge vortex. Because the helix-pitch angle is about 45°, V_θ is equal to the axial velocity V_a. Mean values of V_a were calculated for four spanwise positions from the data in Fig. 4. Circulation distributions in Fig. 5 were scaled to give equal lift in the middle of the downstroke by equating integrals of the product of circulation and flapping velocity.

Received 26 June; accepted 21 October 1996.

1. Weis-Fogh, T. *J. Exp. Biol.* **59,** 169–230 (1973).
2. Ellington, C. P. *Phil. Trans. R. Soc. Lond. B* **305,** 145–181 (1984).
3. Ennos, A. R. *J. Exp. Biol.* **142,** 49–85 (1989).
4. Dudley, R. & Ellington, C. P. *J. Exp. Biol.* **148,** 53–88 (1990).
5. Dudley, R. *J. Exp. Biol.* **198,** 1065–1070 (1995).
6. Cloupeau, M., Devillers, J. F. & Devezeaux, D. *J. Exp. Biol.* **80,** 1–15 (1979).
7. Wilkin, P. J. *J. Kansas Entomol. Soc.* **63,** 316–328 (1990).
8. Zanker, J. M. & Götz, K. G. *Phil. Trans. R. Soc. Lond. B* **327,** 19–44 (1990).
9. Wilkin, P. J. & Williams, M. H. *Physiol. Zool.* **66,** 1015–1044 (1993).
10. Maxworthy, T. *J. Fluid Mech.* **93,** 47–63 (1979).
11. Edwards, R. H. & Cheng, H. K. *J. Fluid Mech.* **120,** 463–473 (1982).
12. Spedding, G. R. & Maxworthy, T. *J. Fluid Mech.* **165,** 247–272 (1986).
13. Sunada, S., Kawachi, K., Watanabe, I. & Azuma, A. *J. exp. Biol.* **183,** 217–248 (1993).
14. Nachtigall, W. *J. Comp. Physiol.* **133,** 351–355 (1979).
15. Ellington, C. P. *Phil. Trans. R. Soc. Lond. B* **305,** 79–113 (1984).
16. Ellington, C. P. in *Biological Fluid Dynamics* (eds Ellington, C. P. & Pedley, T. J.) *Symp. Soc. Exp. Biol.* **49,** 109–129 (1995).
17. Brodsky, A. K. & Ivanov, V. D. *Zool. Zhurn.* **63,** 197–208 (1984).
18. Brodsky, A. K. & Grodnitsky, D. L. *Ent. Obozr.* **64,** 484–492 (1985).
19. Brodsky, A. K. *J. Exp. Biol.* **161,** 77–95 (1991).
20. Grodnitsky, D. L. & Morozov, P. P. *J. Exp. Biol.* **169,** 143–163 (1992).
21. Grodnitsky, D. L. & Morozov, P. P. *J. Exp. Biol.* **182,** 11–40 (1993).
22. Brodsky, A. K. *The Evolution of Insect Flight* (Oxford Univ. Press, Oxford, 1994).
23. Willmott, A. P., Ellington, C. P. & Thomas, A. L. R. *Phil. Trans. R. Soc. Lond. B* (in the press).
24. Dickinson, M. H. & Götz, K. G. *J. Exp. Biol.* **174,** 45–64 (1993).
25. Dickinson, M. H. *J. Exp. Biol.* **192,** 179–206 (1994).
26. Van den Berg, C. & Ellington, C. P. *Phil. Trans. R. Soc. Lond. B* (in the press).
27. Van den Berg, C. & Ellington, C. P. *Phil. Trans. R. Soc. Lond. B* (in the press).
28. Wu, J. Z., Vakili, A. D. & Wu, J. M. *Prog. Aerospace Sci.* **28,** 73–131 (1991).
29. De Vries, O. *Annu. Rev. Fluid Mech.* **15,** 77–96 (1983).
30. Harris, F. D. *J. Am. Helicopter Soc.* **11,** 1–21 (1966).

ACKNOWLEDGEMENTS. This work was supported by the Science and Engineering Research Council, the Hasselblad Foundation and an EC Human Capital and Mobility grant. We thank R. Holder for building the flapper and R. J. Wootton for designing the wings.

CORRESPONDENCE and requests for materials should be addressed to C.P.E. (e-mail: cpe10@cam.ac.uk).

Altered segmental identity and abnormal migration of motor neurons in mice lacking *Hoxb-1*

Michèle Studer, Andrew Lumsden*, Linda Ariza-McNaughton, Allan Bradley† & Robb Krumlauf

Division of Developmental Neurobiology, MRC National Institute for Medical Research, The Ridgeway, Mill Hill, London NW7 1AA, UK
* Department of Developmental Neurobiology, UMDS, Guy's Hospital, London SE1 9RT, UK
† Department of Molecular and Human Genetics, Howard Hughes Medical Institute, Baylor College of Medicine, One Baylor Plaza, Houston, Texas 77030, USA

SEGMENTATION of the vertebrate hindbrain into rhombomeres is important for the anterior–posterior arrangement of cranial motor nuclei and efferent nerves[1]. Underlying this reiterated organization, *Hox* genes display segmentally restricted domains of expression[2–4], such as expression of *Hoxb-1* (refs 5, 6) in rhombomere 4 (r4). Here we report that absence of *Hoxb-1* leads to changes in r4 identity. In mutant mouse embryos, molecular markers indicate that patterning of r4 is initiated properly but not maintained. Cellular analysis by DiI tracing reveals that the r4-specific facial branchiomotor (FBM) and contralateral vestibuloacoustic efferent (CVA) neurons are incorrectly specified. In wild-type mice CVA neurons migrate from r4 into the contralateral side[7], and we found in lineage analysis that FBM neurons migrate from r4 into r5. In mutants, motor neurons differentiate but the CVA and FBM neurons fail to migrate into their proper positions. Instead, they form a motor nucleus which migrates atypically, and there is a subsequent loss of the facial motor nerve. These results demonstrate that, as a part of its role in maintaining rhombomere identity, *Hoxb-1* is involved in controlling migratory properties of motor neurons in the hindbrain.

Despite numerous studies in which targeted mutations of *Hox* genes have been generated[3], their functional role in hindbrain development remains unclear. Loss of function of *Hoxa-1* results in the deletion of rhombomeres[8–10], suggesting that it controls segmentation, whereas overexpression of *Hoxa-1* (refs 11, 12) or *Hoxb-1* (refs 11–13) induces changes in patterning, which is more consistent with an involvement in conferring rhombomere identity. Because the r4 expression of *Hoxb-1* is unique amongst the *labial* group (reviewed in ref. 4), removal of its function might help to distinguish between these alternatives. Accordingly, we generated two loss-of-function mutations in the *Hoxb-1* locus by homologous recombination in embryonic stem cells (Fig. 1*a*, *b*). For both mutant alleles, heterozygous mice were indistinguishable from wild-type animals, but 98% of homozygotes died within 24 h of birth. We used a polyclonal antibody raised against Hoxb-1 (ref. 13) to confirm the absence of Hoxb-1 in homozygous mutant embryos (Fig. 1*c*).

Our previous studies indicated that the r4 expression of *Hoxb-1* is dependent upon an enhancer with a binding site for labial-related proteins, suggesting that r4 is controlled by an auto- or cross-regulatory loop[13]. Because the r4 expression is not lost in *Hoxa-1* mutants[8–10], we investigated whether *Hoxb-1* itself is required by examining the consequences of loss of Hoxb-1 protein on its own regulation. Transgenic lines carrying an alkaline phosphatase reporter construct (HPAP) under the control of the *Hoxb-1* r4 regulatory region[14] were assayed for reporter expression at 9.5 days post coitum (d.p.c.) in both mutant and wild-type backgrounds (Fig. 1*d–g*). Absence of Hoxb-1 results in the loss of reporter expression specifically in r4, leaving the limb bud staining unaffected (Fig. 1*f*, *g*). Thus r4 expression of Hoxb-1 is strictly dependent on its own product and confirms that direct auto-regulatory mechanisms[13] are an important component of segmental expression.

To investigate whether hindbrain segmentation is affected in *Hoxb-1*$^{-/-}$ mice, we analysed the pattern of segmentally expressed markers. The expression of *Krox20* (ref. 15) and *Sek1* (ref. 16) in r3 and r5, of *kreisler* (ref. 17) in r5 and r6, and of *Sek2* (refs. 18, 19) in r4 was not altered in early stages (Fig. 2*a–f*; data not shown), and the relative size of the rhombomeres appeared normal. Therefore, the initial sequence of events leading to the generation and molecular patterning of r4 and neighbouring rhombomeres does not depend on *Hoxb-1*.

In contrast, markers expressed in r4 from 8.25 d.p.c. onwards, a period coinciding with the upregulation of *Hoxb-1* in r4, did show alterations. In 8.5 d.p.c. embryos (7–9 somites) mutants have no expression of *Wnt8* (ref. 20) in r4 (Fig. 2*g*, *h*). The antisense strand of *Hoxb-3* is expressed in r3 and more posteriorly, with high levels in r4 and r6 (Fig. 2*i*)[21], and *CRABPI* (refs 22, 23) is expressed at low levels in r2 and r3, with high levels in r4 to r6 (Fig. 3*k*). In homozygous mutant embryos, both these probes show a specific lack of upregulation in the r4 domain, although other regions are unaltered (Fig. 2*j*, *l*).

We then examined whether these alterations reflect a change in segmental identity. To assay for r2 characteristics, we generated a transgenic line containing an HPAP reporter gene under control